Wiley Online Library

Early View publication on www.wileyonlinelibrary.com
(issue and page numbers not yet assigned;
citable using Digital Object Identifier – **DOI**)

Laser Photonics Rev., 1600299 (2017) / **DOI** 10.1002/lpor.201600299

LASER & PHOTONICS REVIEWS

Abstract Metasurfaces, which consist of resonant metamaterial elements in the form of two-dimensional thin planar structures, retain great capabilities in manipulating electromagnetic wave and potential applications in modifying interaction with fluorescent molecules. The metasurfaces with magnetic responses are favorable to weakening fluorescence quenching while less investigated in controlling fluorescence. In this paper, we demonstrate control over fluorescence emission by engineering the magnetic and electric modes in plasmonic metasurfaces consisting of 45-nm-thick gold split-ring-resonators (SRRs). The fluorescence emission exhibits an enhancement factor of ~18 and is predominantly x-polarized with assistance of the magnetic mode excited by oblique incidence with an x-polarized electric field. The magnetic and electric modes excited by oblique incidence with a y-polarized electric field contribute to the rotation of emission polarization with respect to the incident polarization. The results demonstrate manipulating the interaction of fluorescent emitters with different resonant modes of the SRR-based metasurface at the nanoscale by the polarization of incident light, providing potential applications of metasurfaces in a wide variety of areas, including optical nanosources, fluorescence spectroscopy and compact biosensors.

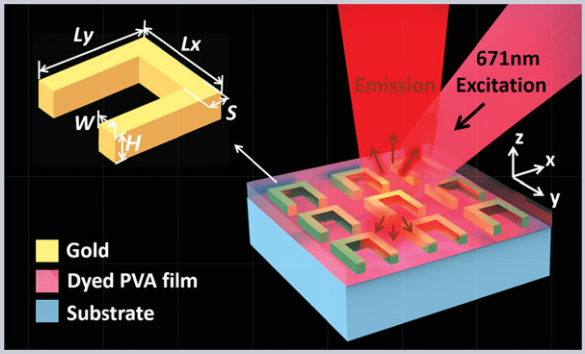

ORIGINAL PAPER

Controlling fluorescence emission with split-ring-resonator-based plasmonic metasurfaces

Si Luo, Qiang Li*, Yuanqing Yang, Xingxing Chen, Wei Wang, Yurui Qu, and Min Qiu

1. Introduction

Metallic nanostructures show the ability to locally confine and enhance the electromagnetic field at the metal-dielectric interfaces mediated by surface plasmon polaritons (SPPs) [1]. Such property is beneficial for enhancing scattering and absorption in the close proximity of the metallic nanostructures [2–4]. If fluorescent molecules are placed close to the metallic nanostructures, their interaction with local SPPs can modify their radiated emission [5–7]. This modification can result in a high quantum yield, an increased radiative decay rate and corresponding bright fluorescence emission [8, 9], which is usually termed as the plasmon-enhanced fluorescence effect. The plasmon-enhanced fluorescence effect plays an important role in optical sensing and imaging [10], biochemical detection [11] and medical measurement [12].

For plasmon-enhanced single-molecule fluorescence, over 100-fold enhancement of the intensity has been demonstrated by exploiting nanocubes [9], bowtie antennas [13], nanoparticles [14], nanoapertures [15,16], nanoprisms [10], etc. These plasmonic nanostructures possess 'hot spots' with ultra-small mode volumes, in which the local electric fields are significantly enhanced and interact efficiently with the single fluorescent molecule. Thereby, strong far-field radiation and high quantum yields of the single fluorescent molecule can be obtained [17–19]. The plasmon-enhanced large-area fluorescence has also been demonstrated on layered metal films [20–22], and grated metal or dielectric surfaces [23–27], where an area-average fluorescence enhancement factor of about 10–200 is generally achieved. Metasurfaces are two-dimensional ultrathin planar structures consisting of resonant metamaterial elements (also termed as "antennas") [28, 29]. The metasurfaces provide an avenue for realizing a new generation of flat optical elements with unique functionalities such as frequency selectivity, wavefront shaping and polarization control. Plasmonic metasurfaces with nanorods [30], nanoparticles [31], nanocolloids [32], nanohole arrays [33], half-shell arrays [34], tilted nanopillars [35], gradient dimmers [36], rectangular nanoholes [37] and hybrid plasmonic-photonic crystals [38] have been introduced to enhance the fluorescence intensity in large areas. Split-ring-resonator-based (SRR-based) plasmonic metasurfaces have been widely used for their fruitful electric and magnetic modes in a variety of applications such as quantum light sources [39, 40], Raman spectroscopy [41] and optical sensors [42–45]. In addition, the SRR-based plasmonic metasurfaces play an important role in second harmonic generation because of their strong local field enhancements associated with both the fundamental and high order magnetic resonances [46–50]. The electric and magnetic modes supported by the SRR-based metasurfaces have also been utilized to study their interaction with quantum dots at normal incidence. The averaged emission is improved with a factor of only 1.6 with magnetic modes at polarization

State Key Laboratory of Modern Optical Instrumentation, College of Optical Science and Engineering, Zhejiang University, Hangzhou, 310027, China

*Correspondence: E-mail: qiangli@zju.edu.cn

© 2017 by WILEY-VCH Verlag GmbH & Co. KGaA, Weinheim

perpendicular to the side arms while no enhancement is obtained at polarization parallel to the side arms [42]. In addition, fluorescence polarization properties and controlling fluorescence by changing the incident polarizations still need to be explored. The magnetic mode is favorable to weakening emission quenching because its electric field shows weaker distance dependence compared to that of the electric mode [51]. The SRR-based metasurfaces with electric and magnetic responses are much less investigated in controlling fluorescence. Therefore, it is of vital importance to explore the plasmon-enhanced fluorescence based on SRR-based metasurfaces.

In this paper, control over fluorescence radiation based on the SRR-based metasurface is reported. At oblique incidence, the magnetic modes are excited with both x- and y-polarized electric fields. An area-average fluorescence enhancement factor of 18 is achieved even at 77° oblique incidence with an x-polarized electric field when the fluorescent molecules couple with the magnetic modes of the SRR-based metasurface. Another magnetic mode, which can only be excited at oblique incidence with a y-polarized electric field, can achieve an area-average fluorescence enhancement factor of 8 together with an electric mode and the emission polarization is not the same as the incident polarization. By controlling the interaction of fluorescent molecules with different resonant modes of the SRR-based metasurface, the radiation can be engineered in a controllable fashion. This result substantially broadens the scope of radiation control at the nanoscale based on metasurfaces, paving a way towards tunable nanophotonic and nanoplasmonic devices.

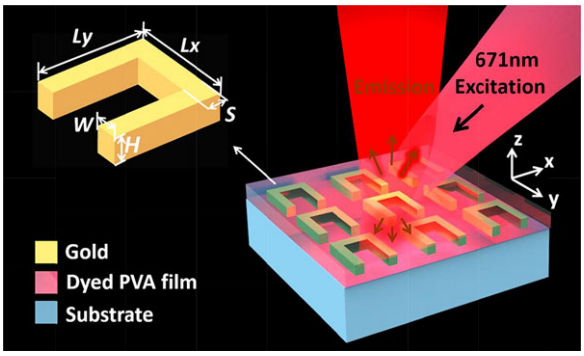

Figure 1 A schematic of control over fluorescence emission with the SRR-based metasurface. A gold SRR-based metasurface on a mica substrate is coated with a 20-nm-thin PVA film containing dye molecules (Rh 800). The thickness of the gold array is $H =$ 45 nm and other parameters of individual resonators are $Lx =$ 155 nm, $Ly = 145$ nm, $W = 45$ nm and $S = 70$ nm. The periods of the array are 240 nm and 250 nm in the x and y directions, respectively.

2. Materials and Methods

2.1. Preparation of dyed SRR-based metasurface

A 45-nm-thick gold film is coated on a mica substrate by electron beam evaporation. The SRR-based metasurface is fabricated with a focused ion beam. To make these dye molecules homogeneously dispersed in the SRR-based metasurface, the Rh 800/water solution (2 mM) is mixed with polyvinyl alcohol (PVA) (Sigma Aldrich; MW 16000–23000) aqueous solution (20 mg/ml) with a volume ratio of 2:1. After that, the mixed solution is spin-coated (first 6 s with 800 rpm and then 60 s with 7000 rpm) onto the SRR-based metasurface. The thickness of this dyed PVA film determined by a step profiler is about 20 nm.

2.2. Optical measurements

In the experimental set-up for measuring the fluorescence emission (Fig. S1), a 671 nm continuous-wave laser is focused on the sample with an optical lens with a focal length of 200 mm from the PVA side to excite the dye molecules at oblique incidence. A linear polarizer (P_1) and a half-wave plate are inserted into the incident path to control the incident polarization. For the fluorescence measurement, the emission is collected by a $\times 50$ objective (NA $= 0.5$) from the same side and detected by a spectrometer (Ocean Optics, QE65 Pro) and a camera. A long-pass filter (Thorlabs FELH0700) is introduced in the detection path to remove the residual excitation light from the fluorescence emission. Another linear polarizer (P_2) can also be inserted after the filter to allow for selective collection of the fluorescence in different polarizations. The integration time of the spectrometer is set as 1 s and the exposure time of the camera is 10 s to maximize the signal-to-noise ratio.

2.3. Numerical Simulations

Finite-difference time-domain method (FDTD Solutions v8.13, Lumerical) is used to compute the optical responses of the SRR-based metasurface. The dielectric function of gold is taken from the book by Palik [52]. In the simulation for SRR unit cells, Bloch periodic boundary conditions are imposed along both x and y directions. A plane-wave pulse is used to illuminate the whole structure and the finest grid size is fixed at 5 nm in all three directions. The near-field electric and magnetic fields are recorded in the x-y plane 5 nm above the SRR-based metasurface. The transmission spectra for the x- and y-polarized incidence are calculated by integrating the flux of the Poynting vectors in planes below the SRR-based metasurface.

3. Results and Discussion

3.1. Mode analysis

Figure 1 shows a schematic of control over the fluorescence emission with the SRR-based metasurface. The SRR-based

© 2017 by WILEY-VCH Verlag GmbH & Co. KGaA, Weinheim

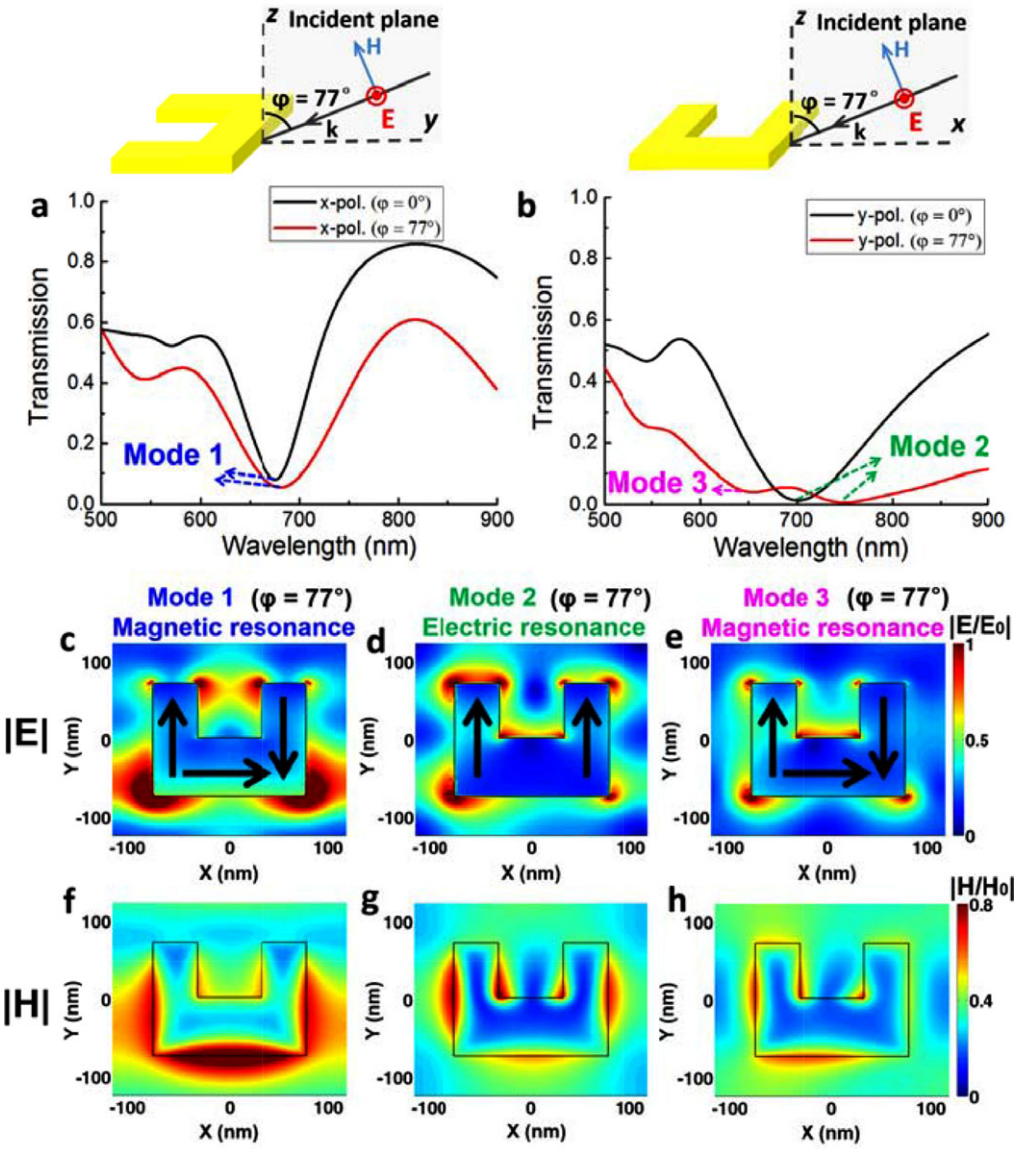

Figure 2 Simulated transmission spectra and resonant field distributions of the SRR-based metasurface. (a, b) Simulated transmission spectra at x- and y-polarized incidence. The black and red lines denote the incident angles of $\varphi = 0°$ and $\varphi = 77°$, respectively. The locations of resonant modes are marked with arrows. (c-e) Simulated electric field intensity distributions of (c) the magnetic mode (Mode 1) for x-polarized incidence, (d) the electric mode (Mode 2) and (e) the magnetic mode (Mode 3) for y-polarized incidence. The incident angle is $\varphi = 77°$. The black arrows show the schematics of current distributions. (f-h) Simulated magnetic field intensity distributions of the three corresponding modes. The electric and magnetic fields are recorded in x-y planes 5 nm above the SRR-based metasurface.

metasurface with periods of 240 nm (x-direction) and 250 nm (y-direction) is fabricated with a focused ion beam. The lengths of the bottom and side arms (Lx and Ly) are around 155 nm and 145 nm, respectively. The widths of the bottom and side arms (S and W) are around 70 nm and 45 nm, respectively. The fluorescent molecules used in this work are dye Rhodamine 800 (Rh 800) molecules with an absorption maximum at about 680 nm and an emission maximum at around 700 nm (Fig. S4) [53]. The intrinsic quantum yield of the dye is measured in the range of 0.16–0.25 [53, 54]. With optimized structural parameters, the wavelength of the electric and magnetic modes of the SRR-based metasurface matches the emission spectrum of fluorescent molecules.

To unveil the physics behind the fluorescence enhancement, the optical properties of the SRR-based metasurface are theoretically studied. For normal incidence ($\varphi = 0°$) with an x-polarized electric field, the resonance is at 680 nm in the visible light region (Fig. 2a). The resonant wavelength changes slightly when the incident angle φ varies from 0° to 77° (Fig. 2a). For this resonance at oblique incidence ($\varphi = 77°$), an electric quadrupole in the two side arms and an electric dipole in the bottom arm can be

© 2017 by WILEY-VCH Verlag GmbH & Co. KGaA, Weinheim

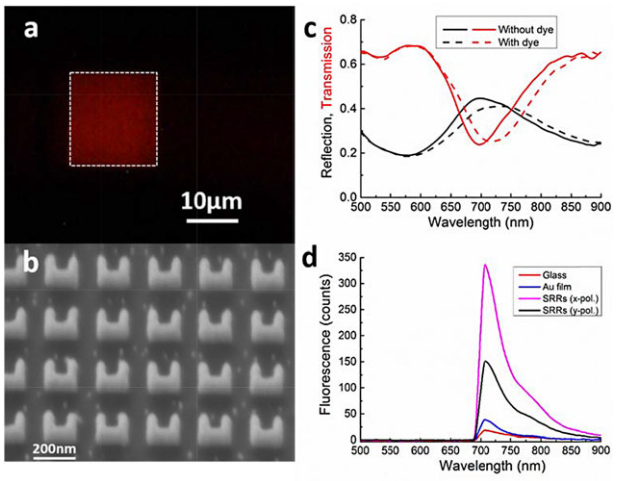

Figure 3 Fluorescence properties of the SRR-based metasurface. (a) A microscopy image of the fluorescence emission excited by a 671 nm laser on the sample at 77° oblique incidence. The boundaries of the SRR-based metasurface is indicated by white dotted lines. (b) A SEM image of a part of the fabricated SRR-based metasurface in (a). (c) Measured transmission and reflection spectra of the SRR-based metasurface under white light illumination without (solid lines) and with (dashed lines) a dyed PVA film coated. (d) Measured enhanced fluorescence spectra of the SRR-based metasurface coated with a dyed PVA film under x-polarized (pink) and y-polarized (black) incidence. Measured fluorescence spectra of dyed PVA films on gold (blue) and glass (red) substrates are provided for references.

distinguished (Fig. 2c). The electric fields are mainly confined around the two outer corners of the bottom arms of the SRR-based metasurface. The corresponding magnetic fields are primarily localized at the outer sides of the three arms of the SRR-based metasurface, forming three magnetic moments (Fig. 2f). This resonant mode (termed as "Mode 1") is therefore referred to as a magnetic mode due to the presence of magnetic moments [55]. For this magnetic mode, its electric and magnetic field distributions are insensitive to the incident angle φ (Fig. S2). This is a high-order magnetic mode and the fundamental one is located at about 1.1 μm in the near-infrared region (Fig. S3).

For normal incidence ($\varphi = 0°$) with a y-polarized electric field, the resonance excited at about 700 nm (Fig. 2b) is characterized by two strong electric dipole moments (Fig. 2d), which is referred to as an electric mode (termed as "Mode 2"). The two induced electric dipoles in the two side arms are symmetric with the same current directions along the side arms. At 77° oblique incidence, the resonance peak of Mode 2 is red-shifted to about 750 nm; the electric and magnetic field distributions are still similar to those at normal incidence (Fig. S2). More importantly, a new resonance at about 650 nm emerges at 77° oblique incidence. Distinct from the two symmetric electric dipoles in the two side arms in Mode 2, this new resonance possesses two anti-symmetric electric dipoles (an electric quadrupole) in the two side arms and their mutual coupling results in the opposite charge polarities in the bottom arm (Fig. 2e). This resonant mode resembles the Mode 1 in the electric and magnetic field distributions except that they are non-symmetric between the two side arms because the symmetry is broken in terms of the two side arms at oblique incidence. Therefore, this mode is referred to as another magnetic mode (termed as "Mode 3").

3.2. Enhanced fluorescence Properties

Transmission and reflection spectra and fluorescence measurement of the SRR-based metasurface are first obtained. The microscope image (Fig. 3a) demonstrates bright fluorescence emission at the SRR-based metasurface (16 μm×17 μm in size), which is clearly distinguishable from the dark background (the non-patterned Au film). The scanning electron microscopy image of the fabricated device illustrates good uniformity of the SRR-based metasurface (Fig. 3b). Transmission and reflection spectra of the SRR-based metasurface are measured with white light at normal incidence without and with a coated dyed PVA film (Fig. 3c). The resonant wavelength of the SRR-based metasurface is around 700 nm without the dyed PVA film. This resonant wavelength slightly shifts (less than 30 nm) after the sample is covered with the dyed PVA film, which is still near the emission center wavelength of the dye molecules. When excited by a 671 nm laser at an oblique incident angle of $\varphi = 77°$, the fluorescence spectrum with an emission peak of around 706 nm from the SRR-based metasurface can be obtained (Fig. 3d). For references, the fluorescence spectra from both the Au and glass substrates coated with the same dyed PVA film (same thickness and dye concentration) are provided (Fig. 3d). The oblique incidence can excite the magnetic modes with both the x- and y-polarized electric fields (see "Mode analysis" part). The oblique incident angle φ is limited to be between 66° to 83° due to the limitation of the numerical aperture and the working distance of the objective used in the experiment (Fig. S1). The fluorescence enhancement factor of the SRR-based metasurface is insensitive to the oblique incident angle φ from 66° to 83° and the incident angle is thereby fixed at φ = 77° throughout this study. The measurement is conducted at excitation power of about 5 mW, which is below the damage threshold of the dye molecules. Under x-polarized incidence, a fluorescence enhancement of approximately 18-fold for the SRR-based metasurface compared to the glass substrate (Fig. 3d) can be obtained. An 8-fold fluorescence enhancement is achieved in comparison with the Au substrate. Under y-polarized incidence, the enhancement factors are ~8-fold and ~3.5-fold compared to the glass and Au substrates, respectively. Therefore, the SRR-based metasurface can distinctly enhance the fluorescence intensities under both polarizations of excitation light at oblique incidence. These results provide good evidence that the fabricated SRR-based metasurface can significantly enhance the fluorescence as compared to conventional planar metal or glass surfaces.

© 2017 by WILEY-VCH Verlag GmbH & Co. KGaA, Weinheim

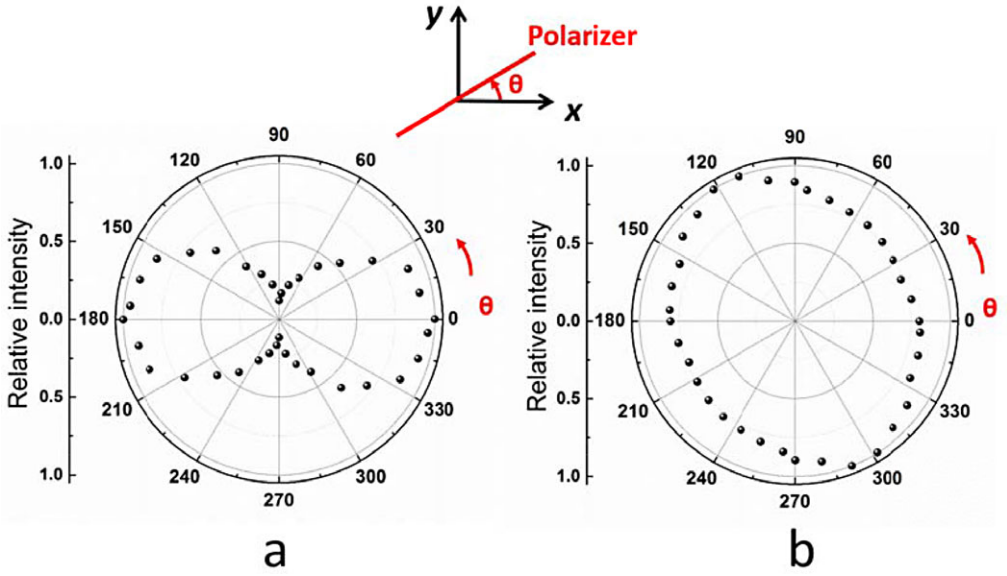

Figure 4 Measured fluorescence intensities at different output polarizations by rotating the polarizer in the detection path. (a) and (b) are for the x- and y-polarized incidence, respectively. Both the incident angles φ are 77°. The fluorescence intensities are normalized to their maximum value for x- and y-polarized incidence, respectively. The fluorescence emission is measured for θ (polarization angle of P_2) changing from -90° (270°) to 90° while the data from 90° to 270° is obtained based on the symmetry of the polarizer.

3.3. Fluorescence polarization properties at x- and y-polarized incidence

In order to explore the fluorescence polarization properties, a linear polarizer P_2 is inserted into the detection path (Fig. S1). By rotating the polarizer (the rotation angle is termed as θ), the fluorescence intensities at different polarizations can be obtained. The fluorescence peak intensities at different polarizations are normalized by their respective maximum for x- and y-polarized incidence (Fig. 4). For the x-polarized incidence (Fig. 4a), the maximum emission intensity polarizes at the same direction as the incident polarization ($\theta = 0°$), consistent with the direction of the induced charge polarity along the bottom arm.

For the y-polarized incidence (Fig. 4b), the maximum emission intensity polarizes -60° away from the x direction ($\theta = -60°$), indicating that the radiation polarization rotates with respect to the incident polarization. This polarization rotation results from the contribution of the induced charge oscillation in the bottom arm in Mode 3, which radiates with an electric field component orthogonal to the incident polarization. Therefore, x-polarized fluorescence intensities are also strong and the polarization of the maximum fluorescence intensity rotates ($\theta = -60°$) with respect to the y-polarized electric field at oblique incidence. Besides, the fluorescence intensities at different polarizations are not symmetric with respect to the x-z plane (Fig. 4b) due to the geometric asymmetry of the SRR-based metasurface along the x direction. In addition, the fluorescence intensities at different polarizations are not symmetric with respect to the y-z plane. This is because the excited mode distributions (Mode 2 and Mode 3) are not symmetric in the two side arms (Fig. 3d, e, g and h).

To further analyze the fluorescence polarization properties produced by the SRR-based metasurface, an overall degree of linear polarization (DOLP) of the fluorescence can be introduced. $\mathrm{DOLP} = (I_x - I_y)/(I_x + I_y)$, where I_x and I_y are fluorescence intensities of the x and y components, respectively. The DOLP value is 0.78 for the x-polarized incidence and -0.05 for the y-polarized incidence. The negative DOLP value indicates that y-polarized fluorescence intensity dominates. Therefore, highly polarized fluorescence with a relative large DOLP value can be obtained at x-polarized incidence; in contrast, the polarization of the fluorescence deviates from the incident polarization at y-polarized incidence because of the combined contribution from both electric and magnetic modes (Mode 2 and Mode 3).

3.4. Controlling fluorescence by changing the incident polarizations

In order to control the fluorescence emission properties, a linear polarizer P_1 is inserted into the incident path while the incident angle φ is maintained at 77° (Fig. S1). By rotating the polarizer (the rotation angle is termed as α), both the x- and y-polarized normalized fluorescence intensities (polarizer P_2 is still in the detection path) can be obtained (Fig. 5). For incidence at the y-z plane, the y-polarized fluorescence is much weaker than the x-polarized fluorescence, which is consistent with the results corresponding to $\alpha = 0°$ in Fig. 4a. Besides, for the x-polarized fluorescence, the maximum and the minimum

© 2017 by WILEY-VCH Verlag GmbH & Co. KGaA, Weinheim

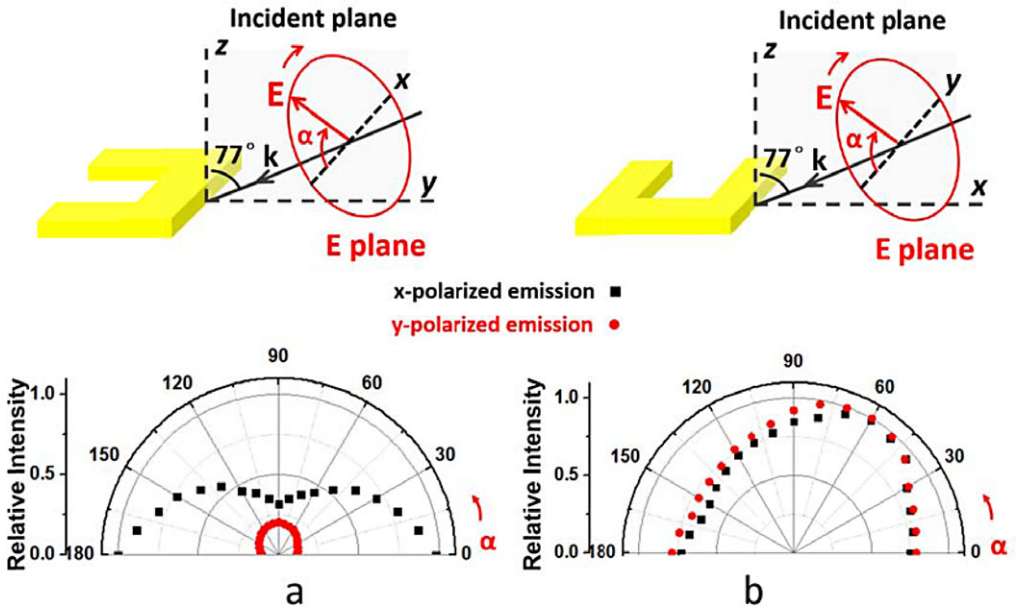

Figure 5 Measured fluorescence intensities (both x- and y-polarized) at different incident polarizations by rotating the polarizer in the incident path. (a) and (b) are for incident wave-vectors in y-z and x-z planes, respectively. Both the incident angles φ are 77°. The black and red dots denote the x- and y-polarized fluorescence intensities, respectively.

occur at $\alpha = 0°$ and $\alpha = 90°$, respectively. The DOLP values can be modified from 0.21 to 0.78 with the incident polarization α varying from 90° to 0° (180°). For incidence at the x-z plane, both x- and y-polarized fluorescence shows slight differences in intensities, resulting in close to zero DOLP values. The results furtherly show using different incident polarizations to control the fluorescence of the SRR-based metasurface based on the interplay of different resonant modes with the fluorescent molecules.

In this paper, the fluorescence emission enhanced by the SRR-based metasurface is realized at both x- and y-polarized incidence. Especially, the fluorescence enhancement factor is as large as 18 at x-polarized incidence. The fluorescence enhancement factor can be qualitatively predicted by calculating the electric field enhancement. The fluorescence enhancement factor (EF) is related to the electric field enhancement by $EF \propto (\frac{E}{E_0})^2_{671}(\frac{E}{E_0})^2_{706}$ [56], where $(\frac{E}{E_0})^2$ represents the electric field enhancement in the PVA layer on the SRR-based metasurface (E) compared to that on the glass substrate (E_0), the subscripts 671 and 706 represent the excitation and emission center wavelength, respectively. The experimental fluorescence enhancement factors are lower than the calculated electric field enhancements (Table S1), which can be attributed to the following factors: the imperfections induced in fabricating the SRR-based metasurface and the rough surface profiles of the PVA layer (Table S2). The experimental fluorescence enhancement factors can be further enhanced by using atomically flat single-crystalline gold film [57] and optimizing the structural parameters to improve the electric field enhancements of the resonant modes. Although the effect of the SRR-based plasmonic metasurface on the fluorescent molecules' lifetime is not studied here, it is expected that the lifetime will decrease because of the spectral overlap between the fluorescence and the localized SPPs. The lifetime is usually insensitive to the number of the fluorescent molecules, the incident intensity or the collection efficiency [58].

5. Conclusions

In conclusion, the control over the fluorescence emission with SRR-based plasmonic metasurfaces is demonstrated. At oblique incidence, both x- and y-polarized excitation can excite the magnetic modes to enhance the fluorescence. For x-polarized incidence, the fluorescence is enhanced by a factor of ~18 because of the magnetic mode. The fluorescence emission is mainly polarized along the same direction as the incident polarization, showing a high degree of linear polarization. For y-polarized incidence, the fluorescence is enhanced by a factor of ~8 resulting from the magnetic mode only excited under oblique incidence. The polarization of the fluorescence deviates from the incident polarization because of the combined contribution from both electric and magnetic modes. The fluorescence assisted by SRR-based metasurface can be controlled by changing the incident polarizations from different incident planes. The results provide an avenue for enhanced excitation of nanoscale emitters with metasurfaces and thereby may open up potential applications of metasurfaces in a wide variety of areas, including optical nanosources, fluorescence spectroscopy and compact biosensors.

© 2017 by WILEY-VCH Verlag GmbH & Co. KGaA, Weinheim

Supporting Information

Additional supporting information may be found in the online version of this article at the publisher's website.

Acknowledgements. This work is supported by the National Natural Science Foundation of China (Grant Nos. 61425023, 61575177, 61275030 and 61235007).

Received: 7 November 2016, **Revised:** 16 January 2017, **Accepted:** 6 March 2017

Published online: 29 March 2017

Key words: Metasurface, plasmon-enhanced fluorescence, emission control, magnetic resonance.

References

[1] M. Pelton, Nat. Photon. **9**, 427–435 (2015).
[2] Y. Qu, Q. Li, H. Gong, K. Du, S. Bai, D. Zhao, H. Ye, and M. Qiu, Adv. Opt. Mater. **4**, 480-486 (2016).
[3] G. Lu, Y. Wang, R. Y. Chou, H. Shen, Y. He, Y. Cheng, and Q. Gong, Laser Photonics Rev. **9**, 530–537 (2015).
[4] X. Chen, H. Gong, S. Dai, D. Zhao, Y. Yang, Q. Li, and M. Qiu, Opt. Lett. **38**, 2247-2249 (2013)
[5] Y. Shen, T. He, W. Wang, Y. Zhan, X. Hu, B. Yuana, and X. Zhou, Nanoscale **7**, 20132–20141 (2015).
[6] Y. Jin and X. Gao, Nat. Nanotechnol. **4**, 571–576 (2009).
[7] R. Faggiani, J. Yang, and P. Lalanne, ACS Photonics **2**, 1739–1744 (2015).
[8] D. Darvill, A. Centeno, and F. Xie, Phys. Chem. Chem. Phys. **15**, 15709–15726 (2013).
[9] G. M. Akselrod, C. Argyropoulos, T. B. Hoang, C. Ciracì, C. Fang, J. Huang, D. R. Smith, and M. H. Mikkelsen, Nat. Photonics **8**, 835–840 (2014).
[10] K. Munechika, Y. Chen, A. F. Tillack, A. P. Kulkarni, I. J. L. Plante, A. M. Munro, and D. S. Ginge, Nano Lett. **10**, 2598–2603 (2010).
[11] Y. Wang, L. Wu, T. I. Wong, M. Bauch, Q. Zhang, J. Zhang, X. Liu, X. Zhou, P. Bai, J. Dostalek, and B. Liedberg. Nanoscale **8**, 8008–8016 (2016).
[12] M. Y. Berezin and S. Achilefu, Chem. Rev. **110**, 2641–2684 (2010).
[13] A. Kinkhabwala, Z. Yu, S. Fan, Y. Avlasevich, K. Mullen, and W. E. Moerner, Nat. Photonics **3**, 654–657 (2009).
[14] D. Punj, M. Mivelle, S. B. Moparthi, T. S. van Zanten, H. Rigneault, N. F. van Hulst, M. F. Garcıa-Parajo, and J. Wenger, Nat. Nanotechnol. **8**, 512–516 (2013).
[15] H. Aouani, O. Mahboub, N. Bonod, E. Devaux, E. Popov, H. Rigneault, T. W. Ebbesen, and J. Wenger, Nano Lett. **11**, 637–644 (2011).
[16] R. Regmi, A. A. Al Balushi, H. Rigneault, R. Gordon, and J. Wenger. Sci. Rep. **5**, 15852 (2015).
[17] N. Livneh, M. G. Harats, S. Yochelis, Y. Paltiel, and R. Rapaport, ACS Photonics **2**, 1669–1674 (2015).
[18] M. P. Backlund, A. Arbabi, P. N. Petrov, E. Arbabi, S. Saurabh, A. Faraon and W. E. Moerner, Nat. Photonics **10**, 459–462 (2016).
[19] I. M. Hancu, A. G. Curto, M. Castro-Lopez, M. Kuttge, and N. F. van Hulst, Nano Lett. **14**, 166–171 (2013).
[20] T. Neal, K. Okamoto, and A. Scherer, Opt. Express **13**, 5522–5527 (2005).
[21] R. Badugu, H. Szmacinski, K. Ray, E. Descrovi, S. Ricciardi, D. Zhang, J. Chen, Y. Huo, and J. R. Lakowicz, ACS Photonics **2**, 810–815 (2015).
[22] T. Hartsfield, M. Gegg, P. H. Su, M. R. Buck, J. A. Hollingsworth, C. K. Shih, M. Richter, H. Htoon, and X Li, ACS Photonics **3**, 1085–1089 (2016).
[23] Y. J. Hung, I. I. Smolyaninov, C. C. Davis, and H. C. Wu, Opt. Express **14**, 10825–10830 (2006).
[24] J. J. Jiang, F. Xu, Y. B. Xie, X. M. Tang, Z. Y. Liu, X. -J. Zhang, and Y. -Y. Zhu, Opt. Lett. **38**, 4570–4573 (2013).
[25] E. Hwang, I. I. Smolyaninov, C. C. Davis, Nano Lett. **10**, 813–820 (2010).
[26] Y. Jiang, H. Y. Wang, H. Wang, B. R. Gao, and Y. W. Hao, J. Phys. Chem. C **115**, 12636–12642 (2011).
[27] K. Tawa, H. Hori, K. Kintaka, K. Kiyosue, and Y. Tatsu, Opt. Express **16**, 9781–9790 (2008).
[28] A. E. Minovich, A. E. Miroshnichenko, A. Y. Bykov, T. V. Murzina, D. N. Neshev, and Y. S. Kivshar, Laser Photonics Rev. **9**, 195–213 (2015).
[29] H. Zhao, Y. Yang, Q. Li and M. Qiu, Appl. Phys. Lett. **103**, 261108 (2013).
[30] X. Meng, A. V. Kildishev, K. Fujita, K. Tanaka, and V. M. Shalaev, Nano Lett. **13**, 4106–4112 (2013).
[31] J. Zhang and J. R. Lakowicz, Opt. Express **15**, 2598–2606 (2007).
[32] S. Park, S. W. Lee, S. Jeong, J. H. Lee, H. H. Park, D. -G. Choi, J. –H. Jeong, and J. –H. Choi, Nanoscale. Res. Lett. **5**, 1590–1595 (2010).
[33] J. Li, J. B. Xu, and H. C. Ong, Appl. Phys. Lett. **94**, 41114 (2009).
[34] C. Farcau and S. Aştilean, Appl. Phys. Lett. **95**, 193110 (2009).
[35] R. Verre, M. Svedendahl, L. N. Odebo, Z. J. Yang, G. Zengin, T. J. Antosiewicz, and M. Kàl, Nano Lett. **16**, 98–104 (2016).
[36] L. Langguth, A. H. Schokker, K. Guo, and A. F. Koenderink, Phys. Rev. B **92**, 205401 (2015).
[37] N. Shitrit, S. Maayani, D. Veksler, V. Kleiner, and E. Hasman, Opt. Lett. **38**, 4358–4361 (2013).
[38] B. Ding, C. Hrelescu, N. Arnold, G. Isic, and T. A. Klar, Nano Lett. **13**, 378–386 (2013).
[39] N. I. Zheludev, S. L. Prosvirnin, N. Papasimakis, and V. A. Fedotov, Nat. Photon. **2**, 351–354 (2008).
[40] S. S. Kruk, M. Decker, I. Staude, S. Schlecht, M. Greppmair, D. N. Neshev, and Y. S. Kivshar, ACS Photonics **1**, 1218–1223 (2014).
[41] G. Sarau, B. Lahiri, P. Banzer, P. Gupta, A. Bhattacharya, F. Vollmer, and S. Christiansen, Adv. Opt. Mater. **1**, 151–157 (2013).
[42] M. Decker, I. Staude, I. I. Shishkin, K. B. Samusev, P. Parkinson, V. K. A. Sreenivasan, A. Minovich, A. E. Miroshnichenko, A. Zvyagin, C. Jagadish, D. N. Neshev, and Y. S. Kivshar, Nat. Commun. **4**, 2949 (2013).
[43] X. Xu, B. Peng, D. Li, J. Zhang, L. M. Wong, Q. Zhang, S. Wang, and Q. Xiong, Nano Lett. **11**, 3232–3238 (2011).
[44] S. Zanotto, C. Lange, T. Maag, A. Pitanti, V. Miseikis, C. Coletti, R. DeglInnocenti, L. Baldacci, R. Huber, and A. Tredicucci, Appl. Phys. Lett. **107**, 121104 (2015).

© 2017 by WILEY-VCH Verlag GmbH & Co. KGaA, Weinheim

[45] B. Paivanranta, H. Merbold, R. Giannini, L. Buchi, S. Gorelick, C. David, J. F. Loffler, T. Feurer, and Y. Ekinci, ACS Nano **5**, 6374–6382 (2011).
[46] M. W. Klein, C. Enkrich, M. Wegener, and Stefan Linden, Science **313**, 502-504 (2006).
[47] F. B. P. Niesler, N. Feth, S. Linden, J. Niegemann, J. Gieseler, K. Busch, and M. Wegener, Opt. Lett. **34**, 1997–1999 (2009).
[48] F. B. P. Niesler, N. Feth, S. Linden, and M. Wegener, Opt. Lett. **36**, 1533-1535 (2011).
[49] S. Linden, F. B. P. Niesler, J. Forstner, Y. Grynko, T. Meier, and M. Wegener, Phys. Rev. Lett. **109**, 015502 (2012).
[50] Y. Zeng, W. Hoyer, J. Liu, S. W. Koch, and J. V. Moloney, Phys. Rev. B **79**, 235109 (2009).
[51] D. N. Chigrin, D. Kumar, D. Cuma, and G. von Plessen, ACS Photonics **3**, 27–34 (2016).
[52] E. D. Palik, Handbook of optical constants of Solids: Academic Press, 1985.
[53] A. Alessi, M. Salvalaggio, and G. Ruzzon, J. Lumin. **134**, 385–389 (2013)
[54] P. Sperber, W. Spangler, B. Meier, and A. Penzkofer, Opt. Quant. Electron. **20**, 395–431 (1988).
[55] J. Proust, N. Bonod, J. Grand, and B. Gallas, ACS Photonics **3**, 1581–1588 (2016).
[56] S. Khatua, P. M. R. Paulo, H. Yuan, A. Gupta, P. Zijlstra, and M. Orrit, ACS Nano **8**, 4440–4449 (2014).
[57] J. Huang, V. Callegari, P. Geisler, C. Bruning, J. Kern, J. C. Prangsma1, X. Wu, T. Feichtner, J. Ziegler, P. Weinmann, M. Kamp, A. Forchel, P. Biagioni, U. Sennhauser, and B. Hecht, Nat. Commun. **1**, 150 (2010).
[58] J. Li, A. V. Krasavin, L. Webster, P. Segovia, A. V. Zayats, D. Richards, Sci. Rep. **6**, 21349 (2016).

© 2017 by WILEY-VCH Verlag GmbH & Co. KGaA, Weinheim